



**Bacterial chemotaxis in static gradients quantified in a biopolymer membrane-integrated microfluidic platform**

Journal:	<i>Lab on a Chip</i>
Manuscript ID	LC-ART-05-2022-000481.R1
Article Type:	Paper
Date Submitted by the Author:	21-Jun-2022
Complete List of Authors:	<p>Hu, Piao; Catholic University of America, Mechanical Engineering  Ly, Khanh; Catholic University of America, Biomedical Engineering  Pham, Phu; Catholic University of America, Mechanical Engineering  pottash, Alex; University of Maryland at College Park  Sheridan, Kathleen; The Catholic University of America, Biomedical Engineering  Wu, Hsuan-Chen; National Taiwan University, Biochemical Science and Technology  Tsao, Chen-Yu; University of Maryland, Institute for Bioscience and Biotechnology Research (IBBR)  Quan, David; University of Maryland, Fischell Department of Bioengineering  Bentley, William; University of Maryland, Fischell Department of Bioengineering  Rubloff, Gary; University of Maryland, Materials Science and Engineering; University of Maryland  Sintim, Herman; Purdue University System, Chemistry  Luo, Xiaolong; Catholic University of America, Mechanical Engineering</p>

## ARTICLE

## Bacterial chemotaxis in static gradients quantified in a biopolymer membrane-integrated microfluidic platform

Received 00th January 20xx,  
Accepted 00th January 20xx

DOI: 10.1039/x0xx00000x

Piao Hu,<sup>a</sup> Khanh Ly,<sup>b</sup> Le P. H. Pham,<sup>a</sup> Alex E. Pottash,<sup>c</sup> Kathleen Sheridan,<sup>b</sup> Hsuan-Chen Wu,<sup>d†</sup> Chen-Yu Tsao,<sup>d</sup> David Quan,<sup>d‡</sup> William E. Bentley,<sup>c,d</sup> Gary W. Rubloff<sup>e</sup>, Herman O. Sintim<sup>f</sup> and Xiaolong Luo<sup>a\*</sup>

Chemotaxis is a fundamental bacterial response mechanism to changes in chemical gradients of specific molecules known as chemoattractant or chemorepellent. The advancement of biological platforms for bacterial chemotaxis research is of significant interest for a wide range of biological and environmental studies. Many microfluidic devices have been developed for its study, but challenges still remain that can obscure analysis. For example, cell migration can be compromised by flow-induced shear stress, and bacterial motility can be impaired by nonspecific cell adhesion to microchannels. Also, devices can be complicated, expensive, and hard to assemble. We address these issues with a three-channel microfluidic platform integrated with natural biopolymer membranes that are assembled *in-situ*. This provides several unique attributes. First, a static, steady and robust chemoattractant gradient was generated and maintained. Second, because the assembly incorporates assembly pillars, the assembled membrane arrays connecting nearby pillars can be created longer than the viewing window, enabling a wide 2D area for study. Third, the *in situ* assembled biopolymer membranes minimize pressure and/or chemiosmotic gradients that could induce flow and obscure chemotaxis study. Finally, nonspecific cell adhesion is avoided by priming the polydimethylsiloxane (PDMS) microchannel surfaces with Pluronic F-127. We demonstrated chemotactic migration of *Escherichia coli* as well as *Pseudomonas aeruginosa* under well-controlled easy-to-assemble glucose gradients. We characterized motility using the chemotaxis partition coefficient (CPC) and chemotaxis migration coefficient (CMC) and found our results consistent with other reports. Further, random walk trajectories of individual cells in simple bright field images were conveniently tracked and presented in Rose plots. Velocities were calculated, again in agreement with previous literature. We believe the biopolymer membrane-integrated platform represents a facile and convenient system for robust quantitative assessment of cellular motility in response to various chemical cues.

### 1. Introduction

Bacteria sense and respond to the changes in chemical concentration gradients, many of which are associated with important biological processes such as inflammation, wound healing, and differentiation.<sup>1-3</sup> Chemotaxis allows bacteria to sense chemical stimuli and move along chemical gradients

specific to their microenvironments. During chemotaxis, bacteria use specific chemoreceptors and regulators to recognize chemicals, transduce these signals and modulate the direction of flagellar rotation enabling swimming in a tumble and run modality. By adjusting the relative run and tumble, over time, cells move towards chemoattractants such as food sources and away from unfavourable environments.<sup>4, 5</sup> The converse occurs as well where bacteria swim away from repellents including toxins. Chemotaxis is an important factor in various applications such as biofilm formation,<sup>6</sup> environmental decontamination,<sup>7</sup> pathogen identification,<sup>8</sup> and drug delivery.<sup>9, 10</sup> A wide range of platforms including capillary assays,<sup>11</sup> static chambers,<sup>10, 12, 13</sup> and swarm plate assays<sup>8</sup> have been developed to investigate bacterial chemotaxis. These conventional methods are well-developed and simple, yet the established chemical gradients are difficult to implement and control. They can be unstable, irreproducible, and difficult to quantify.<sup>14</sup> As such, a variety of microfluidic-based gradient generators have been developed over the past decades contributing advantages in time- and cost-saving, reproducibility, programmability, and stability.<sup>15</sup> Gradients established within microfluidic devices are spatiotemporally controllable and highly reproducible for further chemotactic quantification.

<sup>a</sup> Department of Mechanical Engineering, Catholic University of America, Washington, District of Columbia 20064, United States

<sup>b</sup> Department of Biomedical Engineering, Catholic University of America, Washington, District of Columbia 20064, United States

<sup>c</sup> Fischell Department of Bioengineering, University of Maryland, College Park, MD 20742 United States.

<sup>d</sup> Institute for Bioscience & Biotechnology Research, University of Maryland, College Park, MD 20742 United States.

<sup>e</sup> Department of Materials Science & Engineering, University of Maryland, College Park, MD 20742, United States.

<sup>f</sup> Department of Chemistry, Purdue University, West Lafayette, IN 47907, United States

<sup>†</sup>Current address: Department of Biochemical Science and Technology, National Taiwan University, Taipei 10617, Taiwan

<sup>‡</sup>Current address: National Institute of Diabetes and Digestive and Kidney Diseases (NIDDK), Bethesda, MD 20892, United States

\*Correspondence: [luox@cua.edu](mailto:luox@cua.edu)

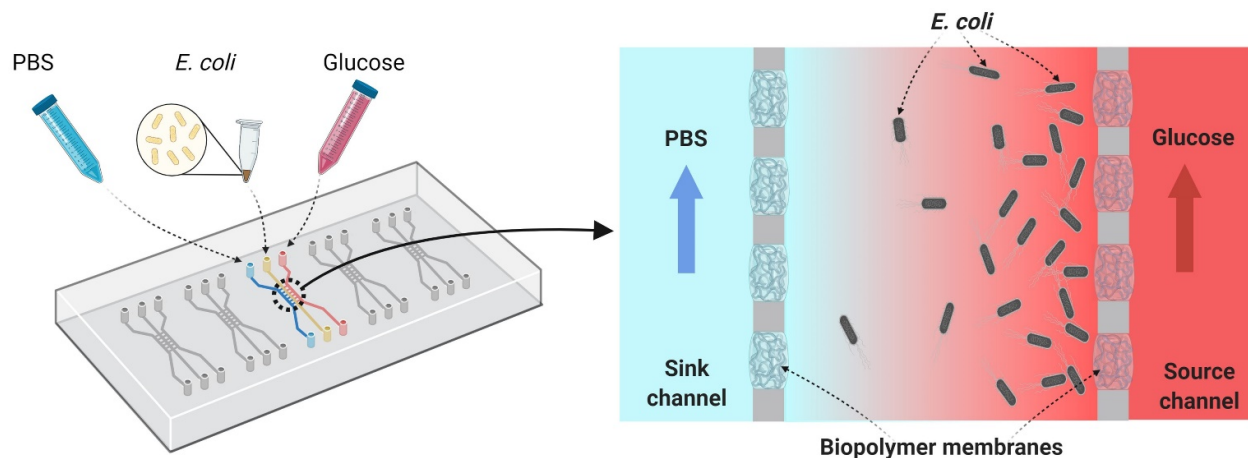
Electronic Supplementary Information (ESI) available: [details of any supplementary information available should be included here]. See DOI: 10.1039/x0xx00000x

There are mainly two types of microfluidic devices for chemotaxis assays: flow-based devices and diffusion-based devices.<sup>16, 17</sup> In flow-based devices, gradients are established across parallel laminar flows in well-designed microfluidic networks including T-shaped,<sup>18</sup> Y-shaped,<sup>19</sup> and Christmas-tree<sup>20</sup> devices. However, the flow-based microfluidic gradient generators can be problematic for shear-sensitive planktonic bacteria, where motions caused by shear stress can complicate the chemotactic quantification process.<sup>2, 21-23</sup> Alternatively, diffusion-based devices generate chemical gradients by the diffusion of biomolecules from source into sink chambers. Static chambers have been used as source and sink reservoirs to avoid shear stress on planktonic bacteria from laminar flows.<sup>10</sup> However, it took hours to establish the gradients with static reservoirs by pure diffusion, and there was little control to maintain a steady gradient over time. More commonly, continuous laminar flows are introduced to maintain constant source and sink concentrations by incorporating flow-resistive components such as membranes or hydrogels.<sup>14, 24-26</sup> While hydrogel-based devices are often comprised of biocompatible materials such as agarose,<sup>22, 27</sup> collagen,<sup>28, 29</sup> or polyethylene glycol (PEG),<sup>30</sup> gradients over a large concentration range are challenging to produce due to the relatively large lateral dimensions of hydrogels (often in the range of a few hundreds of  $\mu\text{m}$ ),<sup>24</sup> or take hours to establish.<sup>31</sup> On the other hand, membrane-based devices offer an enhanced range of chemical gradients because the diffusion of biomolecules through semipermeable membranes can be accommodated from a few to tens of  $\mu\text{m}$ .<sup>24, 32</sup> This is an important aspect of our *in-situ* membrane assembly process.

Several methods have been developed to integrate biopolymer membranes into microfluidic devices.<sup>14, 33-35</sup> Among these, the *in situ* biofabrication of chitosan membranes we developed previously that is based on pH-dependent hydrogel formation is a simple, rapid, and straightforward strategy.<sup>36-38</sup> Chitosan, a derivative of chitin, has been broadly applied for a diverse range of biomedical and tissue engineering applications thanks to its pronounced biocompatibility, biodegradability,

low cost, ease of modification and processing, and non-toxicity.<sup>39-41</sup> Chitosan's solubility is pH-responsive with the transition to hydrogel near pH 6.5, a biologically convenient transition point. That is, it is water-soluble in mildly acidic environments and becomes insoluble or gel-forming when exposed to pH higher than the pKa ( $\sim 6.3$ ) of its primary amine groups.<sup>38, 42, 43</sup> Leveraging this unique property of chitosan, we were able to flow-assemble chitosan membranes *in situ*<sup>36, 37</sup>, and compartmentalized a three-channel polydimethylsiloxane (PDMS) device to generate static gradients with two parallel arrays of chitosan membranes (Scheme 1)<sup>24, 44</sup>. This configuration allows for the establishment of static gradients over a much longer dimension along microchannels and the restriction of pressure-driven flow across microchannels. These parallel membrane arrays address two common issues in current diffusion-based gradient generator devices: pressure-driven breakage and lack of dimension in the gradient area.

We demonstrate the utility of the chitosan membrane-based gradient generator by investigating the well-characterized chemotactic response of *Escherichia coli* (*E. coli*), as shown in Scheme 1, as well as *Pseudomonas aeruginosa* (*P. aeruginosa*) to glucose. We note that bacterial adsorption onto the hydrophobic PDMS channel surfaces was addressed by priming with Pluronic F-127, restoring the hydrophilicity of PDMS and suppressing the non-specific cellular adsorption.<sup>8</sup> Prior to this Pluronic F-127 treatment, chitosan membranes were soaked in glutaraldehyde (GA) solution to crosslink the chitosan membranes, which was demonstrated to have enhanced their anchoring on PDMS to withstand subsequent solution pumping and buffer rinsing without compromising their semi-permeability.<sup>45</sup> Static and steady chemical gradients in the middle channel were generated and well-maintained by the continuous laminar flows of both chemoattractant and buffer solutions in the source and sink channels, respectively. Chemotactic migration of *E. coli* in static glucose gradient was then recorded. We found zero cell adhesion. The chemotactic indexes were reliably quantified, and random walk trajectories



**Scheme 1.** A schematic of a three-channel microfluidic device integrated with biopolymer membranes for chemotaxis study of *E. coli*. PBS buffer (blue) and glucose (red) solutions were flowing in the two side channels to generate a static and steady chemical gradient in the middle channel where bacteria were swimming in response to the static chemokine gradient.

of individual organisms were conveniently tracked using simple brightfield images.

## 2. Materials and Methods

### 2.1 Microfluidic device and chitosan membrane biofabrication

The molds of the three-channel pattern and the add-on vacuum chamber were fabricated using conventional photolithography with negative photoresist SU-8 3035 on 4" silicon wafers. The PDMS microfluidic devices were fabricated using a conventional soft-lithography method by mixing Sylgard 184 and its curing agent (Ellsworth Adhesives, NY, US) at 10:1 ratio, degassed, poured on top of the silicone molds, and cured at 65°C for 4 hours. The solidified PDMS was then peeled off from the mold and cut into desired pieces. The end of each microchannel was punched for input or output. The punched PDMS slab was bonded to a regular microscope glass slide (3" x 1", 1 mm thick, cleaned with methanol and isopropanol, sequentially) using Oxygen Plasma Cleaner PDC-32G (Harrick Plasma, NY, US) as reported.<sup>46, 47</sup> The bonded devices as in Figure 1(a) were then put in an oven at 120°C for at least 24 hours to restore the hydrophobicity of PDMS before the membrane fabrication. Figure 1(b) shows a zoomed-in view of three microchannels with flow-assembled chitosan membranes between PDMS pillars. The depth of the entire microchannel networks was 50 µm. The side microchannels were 500-µm-wide in the tubing connection sections and smoothly curved near the aperture area. The middle microchannel is 400 µm wide at the aperture area, and 300 µm wide connecting to the aperture area. The apertures were 50 µm in all three dimensions and the two arrays of six PDMS pillars on each row between the apertures were 100 µm in length and 50 µm in width. As such, the overall length of the membrane-assembled zone in the middle channel, therefore the well-maintained gradient zone, was 400 µm wide and 950 µm long.

The biopolymer membranes were flow-assembled in three-channel PDMS devices as previously reported.<sup>24, 46</sup> Briefly, chitosan solution (0.5 % w/v, pH ~ 5.5) was introduced into the middle channel and alginate solutions (0.5 % w/v, pH ~ 11.5) were applied in two side channels using PTFE tubing (0.042" OD, Cole Parmer) syringe pumps at 0.5 or 1 µL/min. When all the solutions came to the aperture area, air bubbles were trapped inside the apertures due to the hydrophobicity of the PDMS surface, and the flows were stopped. Any air bubbles were then vacuumed out through the gas permeability of PDMS using an add-on PDMS vacuum chamber connected to a withdrawal syringe,<sup>46</sup> and a thin layer of polyelectrolyte complex membrane (PECM) was instantaneously formed in each aperture upon the contact of the positively charged chitosan and negatively charged alginate. The PECM defined the location where the chitosan membrane would be formed and stopped further mixing of the long chitosan and alginate chains while allowing small ions to freely diffuse through. Then both chitosan and alginate flows were restarted, allowing chitosan membranes to grow upon the PECMs via the diffusion of hydroxyl ions from the high pH alginate side. Within 2 to 3

minutes, the desired membrane thickness of about 30 µm was achieved. The microchannels were manually rinsed with PBS, and the device with chitosan membranes could be stored for weeks inside a humid container at 4°C for future use or be ready for sequent crosslinking of glutaraldehyde (GA) and superficial treatments with Pluronic F-127 before chemotaxis experiments.

### 2.2 Preparation of *E. coli* cells

*E. coli* K-12 strains W3110, BL21 (pCT5 + pET200-GFPuv) that constitutively expresses green fluorescent protein (GFP), and *P. aeruginosa* strain PA01 were used in the chemotaxis assays. A small colony of *E. coli* or *P. aeruginosa* grown on a 1.5% (w/v) Luria broth (LB media, Fisher, Pittsburgh, PA) agar medium was inoculated and grown overnight in a rotary shaking incubator (250 rpm) at 37 °C. The overnight culture was 1% reinoculated into LB medium and grew to an optical density at 600 nm ( $OD_{600}$ ) of 0.5 to 0.7 (mid to late log phase). Cultured cells were centrifuged at 400 g for 5 minutes, then the cell pellet was washed with 1× phosphate-buffered saline (PBS, pH=7.4, Thermo Fisher Scientific) and resuspended in 1× PBS without carbon source. The *E. coli* cells were collected and resuspended in PBS right before chemotaxis experiments to ensure best motility. The GFP expressing BL21 cells were cultured in the same manner as described above.

### 2.3 GA and Pluronic F-127 treatments of chitosan membranes

Chitosan membranes biofabricated in PDMS microchannels were crosslinked with Glutaraldehyde (GA) and primed with Pluronic F-127 as shown in Figure 1(c). GA solution of 10% in PBS (Sigma-Aldrich, St. Louis, MO) was applied in the two side channels for 1 hour to crosslink chitosan membranes to enhance the anchoring onto PDMS.<sup>45</sup> No GA was introduced to the middle channel to avoid the negative effects of residual GA on cells. After 1 hour of GA soaking from the two side channels, all channels were rinsed with PBS first manually with syringe and then at 5 µL/min flow rate for 10 minutes. Then the inner surface of the middle channel was primed with 0.5% w/v Pluronic F-127 for 1 hour. All channels were washed with PBS at 10 µL/min flow rate for 10 minutes. These conditions were developed over many experiments and the resultant devices were good for chemotaxis assays free of nonspecific cell adhesion to the PDMS channel surface.

### 2.4 Gradient generation and introduction of bacteria

To establish the gradient of chemoattractant in the middle channel, the source and sink channels were perfused with laminar flows of 1.0 mM glucose and 1× PBS, respectively, at 1 µL/min flow rate using syringe pumps as shown in Scheme 1. A static and steady gradient was generated within 5 minutes and could be well-maintained for several hours.<sup>24</sup> Freshly prepared *E. coli* or *P. aeruginosa* cells (at  $OD_{600}$  of 0.8 to 1.0 unless specified as in Section 3.2) were introduced into the middle channel by syringe injection, then the microchannel outlet was stopped with a solid metal plug (22 GA, Instech Laboratory Inc.) and the input was inserted with a metal coupler (22 GA, Instech Laboratory Inc.) and sealed with a small piece of parafilm. Thus, there was no external pressure or stress on cells, and the

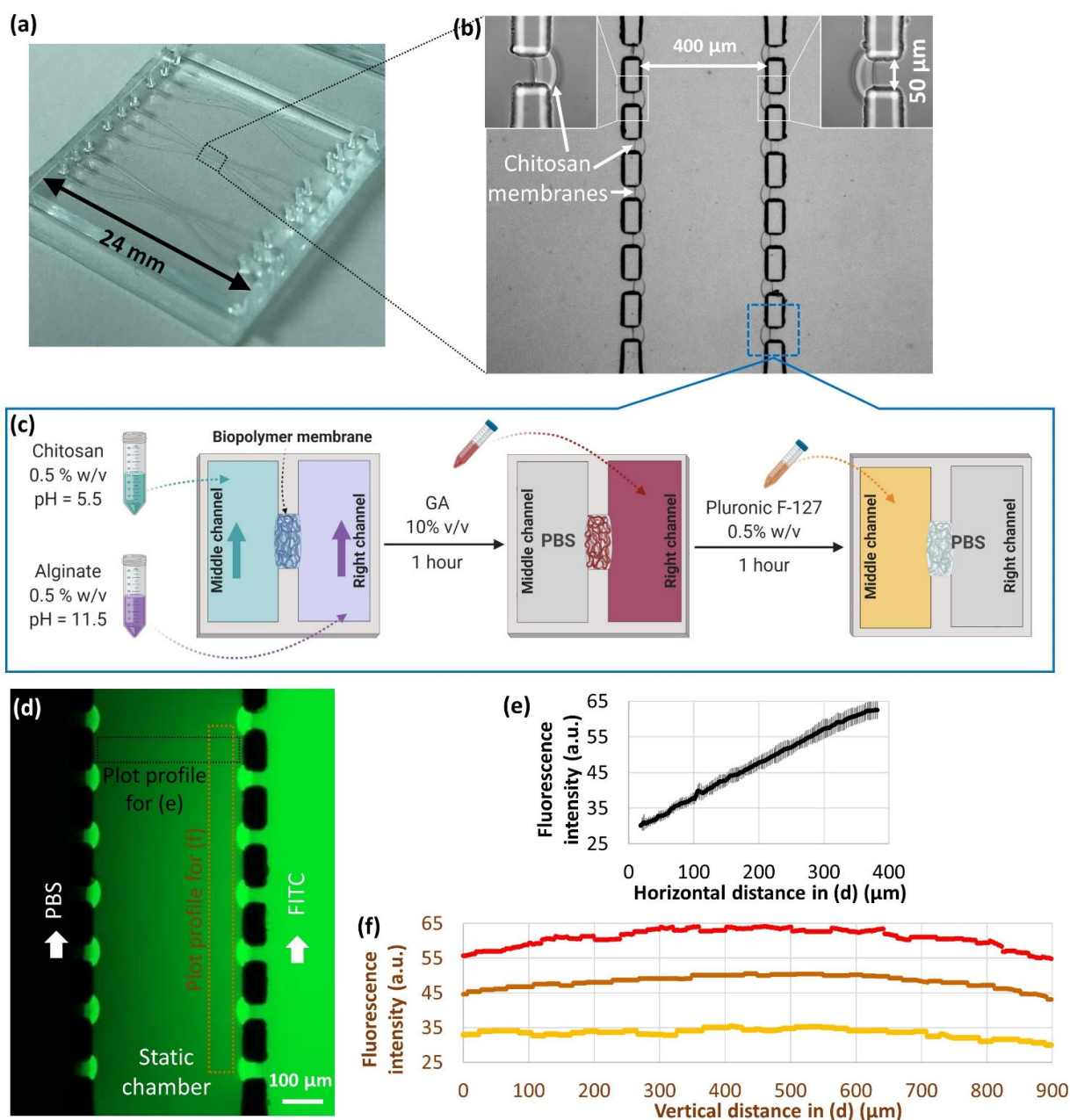


**Figure 1.** Microfluidic platform preparation and chemical gradient generation. **(a)** Three-channel PDMS microfluidic devices bound on a 3"x1" glass slide. **(b)** Zoom-in view of chitosan membranes biofabricated in PDMS apertures between microchannels. **(c)** Semipermeable chitosan membranes were first flow-assembled using chitosan (pH=5.5) and alginate (pH=11.5) solutions to compartmentalize the middle channel. The membranes were then crosslinked and strengthened by filling the side channels with glutaraldehyde (GA) solution for one hour. Next, Pluronic F-127 solution was filled in the middle channel for one hour to prime the polydimethylsiloxane (PDMS) surface to avoid nonspecific cell adhesion. **(d)** Introduction of PBS buffer and fluorescein isothiocyanate (FITC) solutions in the sink and source channels, respectively, generating a FITC gradient in the static middle channel. **(e)** Fluorescence intensity profile across the middle channel, where the black curve and grey error bars represent the average and the standard deviations of fluorescence intensity, respectively, of six horizontal rectangular areas of 350  $\mu\text{m}$  X 80  $\mu\text{m}$  as indicated in (d). **(f)** Three fluorescence intensity profiles of each vertical rectangular area of 80  $\mu\text{m}$  X 900  $\mu\text{m}$  at the left, middle, and right locations along the middle channel from upstream to downstream as indicated in (d).

movement of cells was only stimulated by chemical gradient or chemotactic response. Next, both the glucose and buffer flows were restarted at 1  $\mu\text{L}/\text{min}$  to establish a steady and static gradient in the middle channel for cells, and the chemotactic response of bacterial cells was recorded in real-time under microscope for further analysis. All the chemotaxis and cell migration experiments were performed within 30 minutes at

room temperature, while the doubling time for *E. coli* at room temperature is about 200 minutes, thus bacteria proliferation in the viewing window within 30 minutes was minimum.

## 2.5 Microscopy and image analysis.

The chemotaxis assays consisted of images recorded for 30 minutes using phase contrast or fluorescence light microscopy

unless specified elsewhere. Bright field images for wild type *E. coli* cells and fluorescent images for GFP-expressing *E. coli* cells in Figure 3 and Figure 4 were taken every minute with a Ludesco EXI-310 microscope with 10x (N.A. 0.25, W.D. 7.94 mm) or 20x (N.A. 0.40, W.D. 7.66 mm) LWD objectives and a ProgRes Jenoptik CF USB 2/3" CCD camera (12.5 MP, 14-bit, 2720 x 2048 resolution). Other images and videos were taken using a Zeiss Axio Observer Z1 Inverted Microscope with 10x (N.A. 0.30, W.D. 5.2 mm) or 63x (N.A. 0.75, W.D. 2.2) LWD objectives and an AxioCam HRm Rev. 3 camera (2776 x 2080 resolution, 14-bit/12.5 Hz). Three images from left to right were stitched together without being smoothed to obtain the final images in Figure 2(a)-(ii) and Figure 2(b)-(ii). ImageJ with a Fiji image-processing package (NIH, USA) was used for image processing and data analysis.

All greyscale images were processed with ImageJ. The chemical gradient in Figure 1(e) was processed using the fluorescence intensity profiles of each 350  $\mu\text{m}$  x 80  $\mu\text{m}$  rectangular areas across the channel between opposite PDMS pillars as indicated in Figure 1(d). The average and standard deviations of fluorescence intensity were calculated from six rectangular areas covering the entire gradient zone. The three fluorescence intensity profiles in Figure 1(f) were plotted using each vertical rectangular area of 80  $\mu\text{m}$  X 900  $\mu\text{m}$  at the left, middle, and right locations along the middle channel from upstream to downstream as indicated in Figure 1(d).

Cell optical density in arbitrary units (a.u.) in the presented microfluidic device was measured from transmitted light images as the absorbance of transmission light ( $I$ ) by bacterial cells in the middle channels,  $\text{OD} = |I - I_0|$ , where  $I_0$  is the background light signal without cells.<sup>48, 49</sup> The OD values in Figure 2(c) were calculated using greyscale profile values of each 80  $\mu\text{m}$  X 360  $\mu\text{m}$  rectangle across the channel between opposite PDMS pillars as indicated in Figure 2(a)-(i) and (b)-(i) at 0 and 30 minutes, respectively. The average values and standard deviations of OD were calculated from four rectangles in the viewing windows. Number of cells across the middle channel of the zoom-in images in Figure 2(d) were processed by dissecting the images into 9 sections, 40- $\mu\text{m}$  wide each, and counting the numbers of cells in each section. Fluorescent intensity profiles in Figure 3(a)-(iii) were the average values of five line-profiles across the middle channel covering the entire gradient zone. Cell numbers in Figure 3(b)-(vii) in each time frame was counted using ImageJ. The movements of cells in Figure 5 were tracked and analyzed by TrackMate package in Fiji. The 100 cells trajectories in Figure 5(d) was processed using TumbleScore, an algorithm developed in MATLAB for video analysis<sup>50</sup>, with videos taken at the frame rate of 15 frames/sec.

### 3. Results and discussion

#### 3.1 Static and steady gradient with membranes

The chitosan membrane arrays compartmentalizing the three microchannels were simply fabricated with one simultaneous introduction of alginate and chitosan solutions following previous reports.<sup>24, 46</sup> Both chitosan and alginate are biological

polymers that are stimuli-responsive and easy to assemble in microdevices by tailoring the stimuli such as pH and calcium ions. Utilizing the semi-permeability of the flow-assembled chitosan membranes with porosity in the scale of single nanometers,<sup>36, 37, 44, 45</sup> a static gradient was generated in the middle channel when chemoattractant molecules diffused from source to sink channels. A static chemoattractant gradient was established by applying continuous laminar flows of chemoattractant and buffer in source and sink side channels, respectively, as shown in Figure 1(d). The process took less than 5 minutes and was maintained in steady state as previously reported.<sup>24</sup> Fluorescein isothiocyanate (FITC) was used to visualize the generated chemical gradient of chemoattractant as shown in Figure 1(d). The fluorescent intensity increased smoothly from the sink to the source sides in middle channel.

Specifically, Figure 1(e) shows the plot profile of fluorescence intensity across the middle channel between the opposing PDMS pillars as indicated in Figure 1(d). The average (black curve) and the standard deviations (grey error bars) were calculated from the six rectangular areas of 350  $\mu\text{m}$  x 80  $\mu\text{m}$  horizontally located between each of the six opposing PDMS pillars across the gradient zone (400  $\mu\text{m}$  wide, 950  $\mu\text{m}$  long). The average fluorescence intensity linearly increased from 30 to 63 ( $\pm 2.9$ ) in arbitrary unit (a.u.) with small standard deviations throughout the entire gradient zone. Accordingly, the slope of the horizontal gradient across the middle channel in average was calculated to be 9.4 a.u./100  $\mu\text{m}$  in distance. Figure 1(f) shows three plot profiles of fluorescence intensity of each vertical rectangular area of 80  $\mu\text{m}$  X 900  $\mu\text{m}$  at the left, middle, and right locations along the middle channel from upstream to downstream as depicted in (d). The averages and standard deviations of the three profiles are  $30.0 \pm 2.1$ ,  $47.9 \pm 2.2$ , and  $60.5 \pm 2.6$  a.u. for the left, middle, and right rectangular areas, respectively. Noticeably, these profiles curve down slightly near the upstream and downstream of the middle channel over the 900  $\mu\text{m}$  plotted distance with the difference of 12, 10, and 15 a.u. between its maximum and minimum values for the left, middle, and right profiles, respectively. Accordingly, the slopes of the vertical variations along the middle channel from maximum values in the central locations to the minimal values in the upstream or downstream locations (approximately 450  $\mu\text{m}$  long) were calculated to be 2.6, 2.2, and 3.3 a.u./100  $\mu\text{m}$  for the left, middle, and right profiles, respectively, which are about one third of the slope of the horizontal gradient across the middle channel. Overall, we conclude that the gradient in Figure 1(d) was relatively consistent from the upstream (bottom) to the downstream (top) throughout the 950  $\mu\text{m}$  length.

Besides providing a static gradient over a long dimension between source and sink channels, the chitosan membrane arrays also prevented pressure driven breakage. Noticeably, the brightness associated with the chitosan membranes in Figure 1(d) was due to the reaction between amine reactive FITC and amine-containing chitosan membranes, which would not be a concern with other chemoattractants like glucose.

#### 3.2 Motility of *E. coli* cells in PDMS device

One of the pitfalls in chemotaxis assay is the adherence of cells, especially non-adherent and motile strains. This is particularly problematic in PDMS devices where cell adhesion is common. PDMS is an often-used material in the fabrication of microfluidic chips because it is inexpensive, easily molded, compliant, and biologically benign. But it has an intrinsically high hydrophobicity that can cause nonspecific cell adhesion, thus, complicating chemotaxis analysis. Figure 2 shows how we have dealt with this nonspecific cell adhesion problem. After 30 minutes of chemotactic migration using a cell solution of  $OD_{600} = 5$  under a  $1 \mu\text{m}$  glucose gradient, cells had visibly accumulated near the righthand side (glucose side) of the chemotaxis zone as shown in Figure 2(b). One can compare this to the original ( $t = 0$  minute) uniform distribution of cells in Figure 2(a). The chemotactic migration was obvious as changes in cells

distribution seen in both (i) the overall views and (ii) the zoomed-in views of Figure 2(a) and (b). The distribution of cells in the middle channel was then quantified via ImageJ and plotted in Figure 2(c). Here, we show the normalized OD for the rectangular area across the middle channel between opposite PDMS pillars, and the average and standard deviations of OD were obtained from four rectangular areas covering the entire chemotaxis zone. It was readily apparent that there was an increase in cells towards the glucose source side as shown by the orange solid curve at  $t = 30$  minutes, while the cells were relatively uniform as shown by the blue dotted curve at  $t = 0$  minute. That said, when the bright field images were zoomed in for cell counting, many cells were found stuck to the PDMS ceiling and not moving.

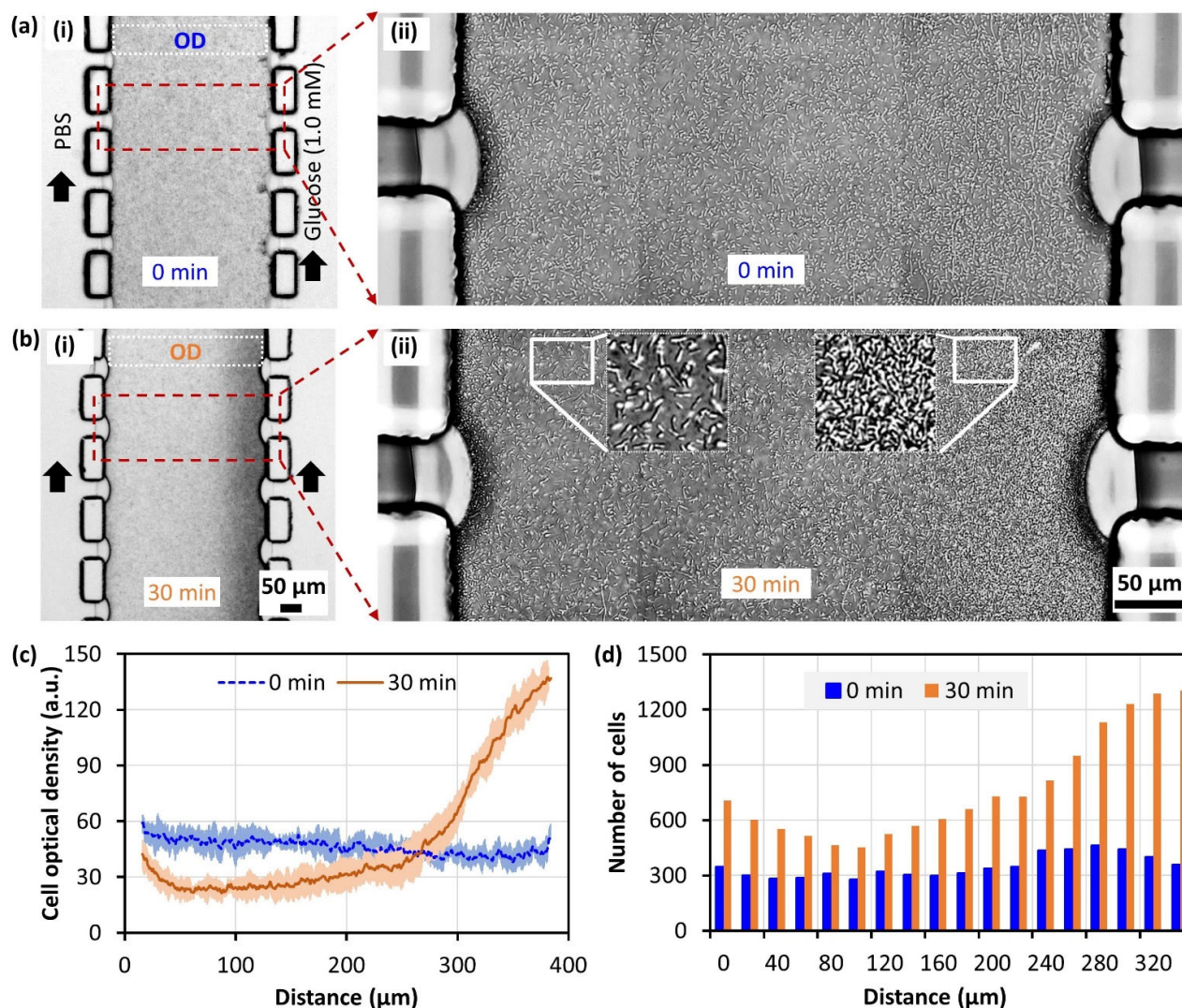


**Figure 2.** Nonspecific cell adhesion on PDMS interfering bacterial chemotaxis study. (a) The original distribution of *E. coli* cells in static condition was homogeneous at the beginning of chemotaxis in both overall view (i) and zoomed-in view (ii). (b) Bacteria migrated towards glucose source after 30 minutes in glucose gradient (i) but many cells adhered to PDMS ceiling in the focus view (ii). (c) Normalized optical density of cells at 0 min in (a)-(i) and 30 min in (b)-(i). The blue dotted curve and the orange solid curve represent the averages of four rectangular areas of  $80 \mu\text{m} \times 360 \mu\text{m}$  as indicated in (a)-(i) and (b)-(i), respectively. Error bars represent the standard deviations of the four measurements at 0 min and 30 min. (d) Number of cells across the middle channel of the zoomed-out images at 0 min in (a)-(ii) and 30 min in (b)-(ii), for which the zoom-in images were dissected into 9 sections,  $40 \mu\text{m}$  wide each, and numbers of cells in each section were counted using ImageJ.

The cell counting results in Figure 2(d) from the high-resolution images in Figure 2(a)-(ii) and 2(b)-(ii) show that the number of cells at 30 minutes was higher than the number of cells at 0 minute throughout the middle channel. Since bacterial proliferation was minimum within the experiment 30 minutes at room temperature and, the higher cell count presumably was due to nonspecific cell adhesion and accumulation to the PDMS surface over time while additional cells might have swum from down- and upstream beyond the observed gradient section. Note that the optical density distribution in Figure 2(c) represents cells throughout the total volume in the microchannel, while the cell count in Figure 2(d) represents cells on the PDMS ceiling of the microchannel. Control experiment of *E. coli* cells without glucose gradient was performed, while cells in upstream of the middle channel outside the viewing window was examined as another control experiment. After 30 min, neither obvious cell migration towards the right nor an increase of cell number in the observation window was observed in both control experiments (Supplemental Figure S1).

We tried several different methods to overcome this cell adhesion problem. First, we found that by subtracting the non-motile cells as background in the post-experimental analysis was helpful. We used this for chemotaxis coefficient calculation.<sup>51</sup> We also tried coating the channel with different biopolymers such as gelatin or collagen and this helped somewhat, alleviated but not completely.<sup>52</sup> We also tried various surface modifying solutions including one with the triblock copolymer Pluronic F-127. We found this restored the superficial hydrophilicity of PDMS and dramatically reduced cell adhesion thanks to its increased surface compatibility and stability over time.<sup>53</sup> For the subsequent experiments, we primed the PDMS microchannels with Pluronic F-127 as it successfully prevented nonspecific cell adhesion, and at the same time did not compromise the anchoring of chitosan membranes onto PDMS. As shown in Figure 1(c), to assist in retaining anchoring strength onto PDMS, chitosan membranes were crosslinked with glutaraldehyde (GA) before the Pluronic F-127 treatment as previously reported.<sup>45</sup> Note that during the GA crosslinking process in Figure 1(c), the middle channel for cell chemotactic migration was filled with PBS buffer in a static condition while the two side channels were filled with GA solution. In this way, we avoided potential negative effects of residual GA on cells since GA is toxic to cells.<sup>54</sup>

After the GA crosslinking and Pluronic F-127 treatment, minimal cell adhesion was observed (Figure 3, Figure 4, and Supplemental Video 2). In these cases, positions of cells at 30 minutes were found to be quite different from those at 0 and 15 minutes. Note that very few cells in the binary images in Figure 3(b)-(v) & (vi) and Figure 3(c) were observed to reside at the same positions over the 0-, 15-, and 30-minute time sequences. Stationary cells could have indicated adhesion to the device surfaces. Instead, *E. coli* cells remained their morphological integrity and apparent motility, a clear indication there was minimal if any cell adhesion to channel surface. Occasionally, some cells did not change their locations over time, presumably nonmotile or dead as no tumbling behaviours were observed. Overall, *E. coli* cell motility was vastly improved

by the combination of static glucose gradient in the device, priming PDMS surface with Pluronic F-127, harvesting bacterial cells in an exponential growth phase, and resuspending cells with no carbon source buffer suppressing cell growth.

Besides addressing the cell adhesion issue, our membrane-integrated platform had avoided the common challenge of shear stress on bacteria in flow-based gradient generators. The source and sink flows in the compartmentalized side channels of our platform do not interact with cells directly in the middle channel. Rather, they worked as an infinite source of chemoattractant and sink via sole chemical diffusions across the semi-permeable chitosan membranes. Moreover, shear stress induced by internal convection flow in the middle channel, caused by buoyancy and diffusioosmosis from transport of chemoattractant and buffer across porous chitosan membranes, was minimal considering the small dimensions of the middle channel width and height (300 and 50  $\mu\text{m}$ , respectively) and low glucose concentration (1 mM) according to a previous report from Gu et al.<sup>55</sup>

It is worth mentioning that while glucose was consumed by the *E. coli* (but not by *P. aeruginosa*) cells, it was continuously replenished from source with continuous flow in the side channel. With dynamic cell migration to the right-side membranes, the glucose gradient might have differed from the original linear profile and a new dynamic equilibrium might have reached around or after 30 minutes. Experimentally it is difficult to measure the time-evolving gradient profile during cell migration. Mathematic simulations could help answer these questions and should be considered in future studies.

In summary, we created a device that generated a stable glucose gradient within minutes so that bacterial cells introduced into the middle channel were monitored both individually and in bulk, enabling the quantification of a variety of chemotaxis parameters.

### 3.3 Bacterial chemotactic migration

Under the static and steady gradient of glucose and with no external constraints on cells, the overall chemotactic migration of *E. coli* cells was clearly observed as in Figure 3 for recombinant *E. coli* expressing GFP (BL21 (pCT5 + pET200-GFPuv)), wild type *E. coli* (W3110), and *P. aeruginosa* strain PA01 cells. The fluorescent *E. coli* cells were uniformly distributed in the middle channel at 0 minute as in Figure 3(a)-(i). After 30 minutes in the glucose gradient, the cell distribution as represented by the fluorescence signal in Figure 3(a)-(ii) showed an obvious skew towards the glucose side. This migration was recorded in discrete images every minute to avoid photobleaching (see Supplemental Video 1). The fluorescence intensity for the indicated sections as in Figure 3(a)-(i) & (ii) was measured and analyzed with ImageJ as shown in Figure 3(a)-(iii). The red curve around  $44.6 \pm 2.8$  a.u. suggested a fairly uniform distribution of cells at  $t = 0$ . As the chemotaxis experiment ensued, the fluorescence profiles became oblique and skewed towards the right half of middle channel. Specifically, the fluorescence level of cells at  $t = 30$  minutes (black curve) increased to 71 a.u. on the glucose side,

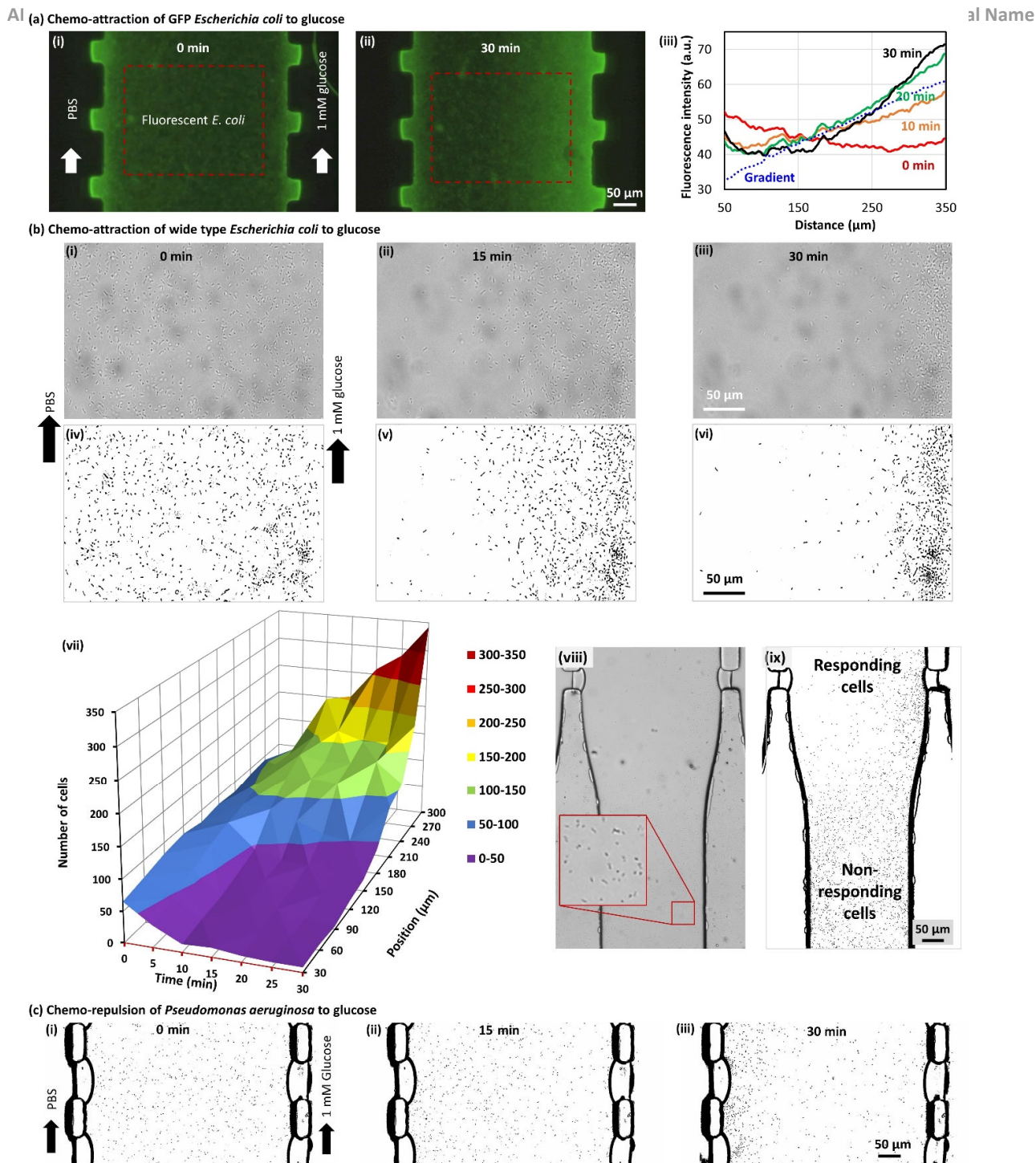


**Figure 3.** Adhesion-free chemotaxis in static glucose gradients. **(a)** Chemo-attraction of green fluorescence protein (GFP)-expressing *E. coli* cells towards 1 mM glucose source. The cells were uniformly distributed in the middle channel at 0 minutes (i) and skewed towards the glucose side after 30 minutes (ii). The change of bacterial distribution over time in static glucose gradient was depicted by plot profiles of fluorescent intensity (the average of five single line profiles) across the middle channel (iii). **(b)** Chemo-attraction of wild type *E. coli* cells towards 1 mM glucose source. The bright field images (i, ii, & iii) and the corresponding binary subtraction (iv, v, & vi) of wild type *E. coli* cells show the representative cell distribution at 0, 15, and 30 minutes during chemotaxis in static glucose gradients. The three-dimensional plot of cells number through in the middle channel over time is shown in (vii) with a peak in red referring to accumulated cells near highest concentration of glucose. For comparison, the bright field image in (viii) and the corresponding binary image in (ix) show distinguishable cell distributions in the gradient section (top portion) vs. the non-gradient section (bottom portion) as the negative control. **(f)** Chemo-repulsion of *Pseudomonas aeruginosa* to 1 mM glucose source. Cells were uniformly distributed at 0 min (left), then slightly skewed to the left at 15 min (middle), then mostly repositioned along the left side near the sink side of the channel.

while it decreased down to around 40 a.u. on the buffer side. Furthermore, the fluorescence of cells at 30 minutes (black

curve) shows a similar tendency as the chemoattractant gradient, which was replotted in Figure 3(a)-(iii) as the dotted

blue curve for reference. Since the duration of the experiment was 30 minutes and there was no growth media – glucose being the only nutrient – there was likely minimal cell growth. This evolution of fluorescence signal over time clearly showed the chemotactic migration of cells towards glucose source.

While GFP-expressing *E. coli* cells are attractive for chemotaxis study as they provide direct visualization of cell migration, enable relatively high signal to noise ratio, and are easily quantified using fluorescence microscopy, there are challenges. The GFP signal is subject to protein and chromophore maturation, configuration states, photobleaching and other issues when observed under continuous imaging conditions. GFP expressing cells do enable visualization, with bright green localized spots on an otherwise dark background. That said, media components are often fluorescent and even in the same wavelengths. We wanted to create systems that are simple to assemble and use. Further experiments were run using wild type instead of GFP-expressing *E. coli* cells. Specifically, brightfield images were processed with simple background subtraction in binary format in ImageJ for quantitative assessments and individual organism tracing analysis<sup>56</sup>.

We next quantified the chemotactic responses using the numbers of *E. coli* cells at different locations through the middle channel (Figure 3(b) and the Supplemental Video 2). Figure 3(b)-(i) to (iii) and (iv) to (vi) show the bright field and binary images of cell distribution, respectively, at three representative time points: (i) at 0 minute where cells were uniformly spread, (ii) at

15 minutes where we found a skewed cell distribution towards the glucose side, and (iii) at 30 minutes where we found even more cell accumulation at the glucose side at 30 minutes. The numbers of counted cells at the different locations and time points were plotted on a three-dimensional surface graph (Figure 3(b)-(vii)). The number of cells found near the glucose side continuously increased from about 60 at 0 minute to a peak of about 340 (i.e., ~ 5.7 times greater) at 30 minutes, while the number of cells near the buffer side decreased from about 60 to about 10 (i.e., ~ 83% decrease) during the same time. These results were easily obtained as the chemotaxis zone was large and not obscured by instrumentation or the sink and source flows. For direct comparison, Figure 3(b)-(viii) and (ix) show the bright field and binary images, respectively, of cell distribution after 30 minutes in and out of static glucose gradients: Cells in the top half of the channel migrated to the right side with higher concentration of glucose; while, as a negative control, cells in the bottom half of channel where the gradient was not established remained uniformly distributed.

To further verify the feasibility and effectiveness of the biopolymer membrane-integrated microfluidic platform for chemotaxis studies, we further tested the chemotactic response of *P. aeruginosa* strain PA01 cells to the static gradient from 1 mM glucose flow in the source channel. Interestingly, the uniformly distributed *P. aeruginosa* cells at 0 minute (Figure 3(c)-(i)) responded to the static glucose gradient and skewed slightly towards the PBS sink side at 15 minutes (Figure 3(c)-(ii)), and skewed furthermore to the PBS side at 30 min (Figure 3(c)-(iii)).

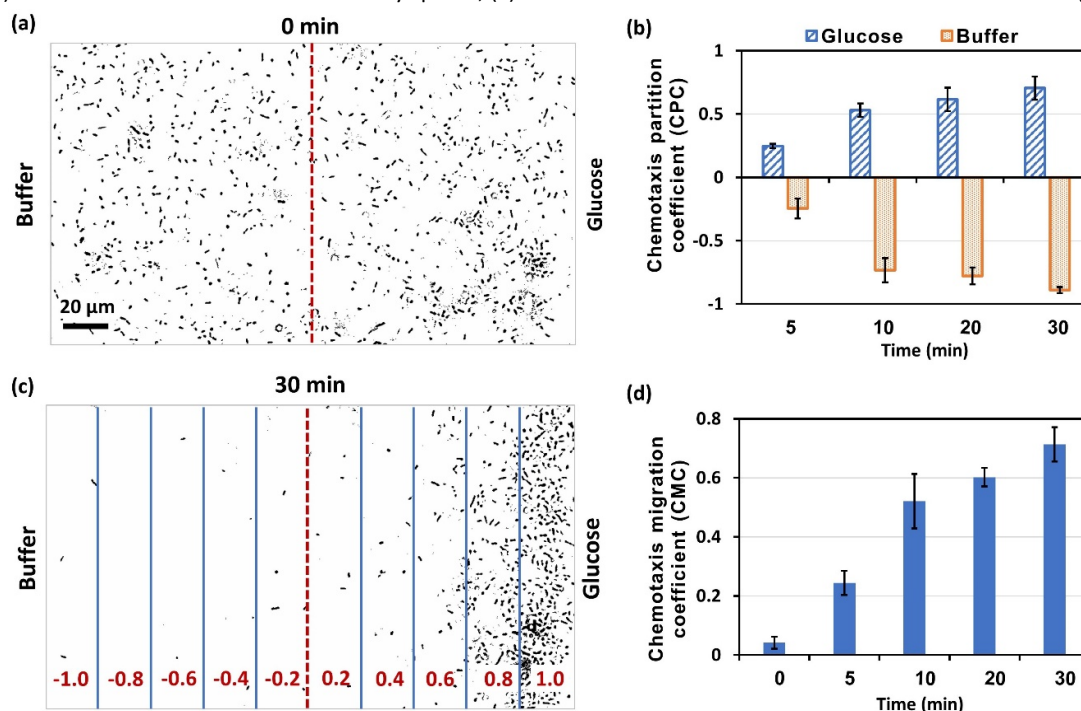


**Figure 4.** Chemotaxis partition coefficient (CPC) and chemotaxis migration coefficient (CMC) for evaluation of chemotactic response. (a) Region of interest was divided into buffer section and glucose section for CPC value calculation. (b) The calculated CPC values showed the attractiveness of glucose to *E. coli* and migrating rate out of the total cells from initially uniform distribution to skewing towards the glucose section. (c) Region of interest was partitioned into 10 columns, each assigned with a specific weighting factor (ranged from -1 to 1 with interval of 0.2) based on the concentration of glucose and travelling distance. (d) The calculated CMC values stood for the average travel distance towards the side of higher glucose concentration area. Error bars were standard deviations of results from three independent experiments.

(iii). Compared to Figure 3(b)-(iii) & (vi) where most *E. coli* cells were chemo-attracted to glucose source after 30 minutes, some *P. aeruginosa* cells in Figure 3(c)-(iii) were lingering in the channel without being chemo-repulsed towards the PBS buffer side. *P. aeruginosa* is a known glucose non-fermenting Gram negative rod<sup>57</sup> that prefers other carbon sources such as organic acids or amino acids rather than glucose<sup>58</sup> because it has limited ability to metabolize sugars<sup>59</sup>. Glucose plays an influential role in the process called carbon catabolite repression (CCR) of *P. aeruginosa* to selectively assimilate a preferred compound among a mixture of several potential carbon sources<sup>58</sup>. As such, sugar administration has been demonstrated as an effective adjunctive therapy in the treatment of *Pseudomonas aeruginosa* pneumonia.<sup>60</sup> Although the detail mechanism of the *P. aeruginosa* chemo-repulsion to glucose gradient is out of the scope in the current study, the results in Figure 3(c) further confirmed that the presented membrane-integrated platform is a useful tool for studying bacterial chemotaxis to well controlled static gradients of interest chemicals.

### 3.4 Quantification of bacterial chemotactic indexes

Chemotaxis was formally characterized by calculating both the chemotaxis partition coefficient (CPC) and chemotaxis migration coefficient (CMC).<sup>18, 61, 62</sup> To calculate CPC, the middle channel was divided into the buffer section and the glucose section as shown in Figure 4(a). The partition of cell number between relatively non-chemotactic buffer section and the chemoattractive glucose section showed the degree of chemotactic response towards chemoattractant. The CPC value was calculated using Equation (1):

$$\text{CPC} = \frac{N_t - N_{\text{ori}}}{N_{\text{ori}}} \quad (1)$$

where  $N_t$  represents the number of cells at a specific time point, and  $N_{\text{ori}}$  stands for the original number of cells at the beginning of chemotaxis. If cells moved from the buffer section to the glucose section, the calculated CPC value for glucose side would be positive due to cell gain and negative for the buffer side due to cell losses. Since *E. coli* cells were uniformly distributed within the middle channel at  $t = 0$ , the original number of cells for both buffer and glucose sections should be nearly the same. Thus, the maximum and minimum values of CPC would be 1 and -1, respectively, which represents a theoretical case wherein all cells moved towards the glucose side.

The calculated CPC values for both buffer and glucose side at different time points of the dynamic chemotactic progressions were plotted in Figure 4(b) with error bars representing standard deviations from three independently replicated experiments. The CPC value for glucose was always positive and increased during chemotaxis measurements, meaning more cells had moved to the glucose side from the buffer side. At 5 minutes, the CPC value of +0.247 for glucose represented a 24.7% increase in cell count in the glucose section. The CPC value then increased to +0.529 at 10 minutes, showing that half of the chemotactic migration from buffer section to the glucose section happened during the first 10 minutes. The average CPC

value for glucose was +0.705 at 30 minutes, representing 70.5% of all the cells were in the glucose section after 30 minutes of chemotaxis. Correspondingly, the CPC for the buffer side was essentially the converse.

The CPC value reflected the overall migration trend of cells from buffer into glucose sections, but this value does not reflect distance that cells had migrated. Thus, the chemotaxis migration coefficient (CMC) was further calculated by dividing the middle channel into 10 equally aligned sections. Each section was assigned with a weighting factor defined by the travelling distance and concentration of chemoattractant as shown in Figure 4(c). The weighting factors were negative for the buffer section and positive for the glucose section, and their absolute values represented the distances from the middle of channel. The CMC weighted with the travelling distance was calculated using Equation (2):

$$\text{CMC} = \frac{\sum N_d * w_d}{\sum N_d} \quad (2)$$

Where  $N_d$  stands for the number of cells at each aliquot, and  $w_d$  is the weighting factor for that aliquot. The sum of the weighted number of cells in all aliquots was divided by the total number of cells that presented cells migration rate under gradient of glucose at specific time points of chemotaxis. The CMC value ranged from -1 to 1 where 1 represented all cells migrated to the rightmost section, having super strong chemo-attractiveness of the chemoattractant, while CMC value of -1 stood for great chemo-repelling ability of the chemorepellent. In the presented glucose gradient for *E. coli* cells, higher value represented higher efficiency of cells migration toward glucose.

The calculated CMC values at different time points of chemotaxis was plotted in Figure 4(d). The CMC value at the beginning of the chemotaxis (0 minute) was close to 0 (+0.042) because the number of cells in all aliquots was about the same and the weighted sum was nearly cancelled out due to inverse weighting factors. The CMC value increased from +0.042 to +0.244 in the first 5 minutes and +0.521 in the first 10 minutes, showing that *E. coli* cells migrated 20.2% of the half channel width in average towards higher concentration of glucose in 5 minutes, and 52.1% of the half-channel width in 10 minutes. The final CMC value at 30 minutes was +0.713, showing that cells moved in average around 71.3% or 107  $\mu\text{m}$  out of the 150  $\mu\text{m}$  half-channel width towards higher concentration of glucose during the 30 minutes of chemotaxis. The increasing CMC values over time represented the continuous chemotactic migration of cells to glucose side under the gradient.

### 3.5 Individually tracked bacteria under chemotaxis

Besides quantifying population-wise chemotactic migration, chemotactic behaviours at single cell resolution were also systematically evaluated to characterize the real-time chemo-attractiveness of glucose to *E. coli* using two analytical approaches. The first approach used TrackMate from Fiji<sup>63</sup> in ImageJ to analyze brightfield images of cells under chemotaxis. The location of cells was captured every second in bright field images and each cell was labelled with an identification number for spatiotemporal tracing to visualize the trajectory plots of

cells. Because most of the cells were in glucose section after 10 minutes according to CPC value, the tracked trajectory paths of cells from 10 to 20 minutes in the glucose section was presented in Figure 5(a), and the migration trajectories were labelled with different colours based on the distance across the gradient direction. The blue paths near left edge were dispersive compared to the red paths near chitosan membranes that were much crowded, as cells accumulated around the right edge with the highest concentration of glucose. Three representative migration paths from 10 to 20 minutes in Figure 5 (b) show that the cells were moving towards right in general while they dangled around in different directions throughout their ways. The movement of these cells between 10 to 11 minutes was zoomed-in in Figure 5(c) with each dot representing the location of cells at each second. The cellular trajectories at every second clearly showed a random walk pattern of bacteria involving a series of runs and tumbles in real-time manner. Even though the zoomed-in walk pattern was relatively random, the overall path obviously directed towards the high chemoattractant (glucose) side.

In the control experiment with no chemical gradient (Figure 5(d), bottom), the distribution of trajectories was uniformly spread from the origin and there was little deviation out of the center of the plot, indicating that “random walk” dominated. In contrast, in the experiment (Figure 5(d), top) where cells were exposed to chemoattractant gradient, the trajectories mostly spread towards the right quadrant, indicating that cell mobility was biased under chemoattractant gradient and chemotactic migration dominated. The calculated average velocities of *E. coli* cells were  $12.1 \pm 2.1 \mu\text{m}$  and  $12.6 \pm 3.1 \mu\text{m}$  for control and experiment, respectively, in agreement with previous literature<sup>64</sup>. Noticeably, the rose plot of the experiment (Figure 5(d), top) shows some drifting towards the top edge, which might be due to some experimental errors or some air bubble-induced flow in the middle channel during video-taking. Nevertheless, the rose plots clearly show the chemotactic migration regardless of some flow disturb in the direction perpendicular to the glucose gradient, thanks to the overall consistent gradient from upstream to downstream throughout the chemotaxis area of  $950 \mu\text{m}$  length between the

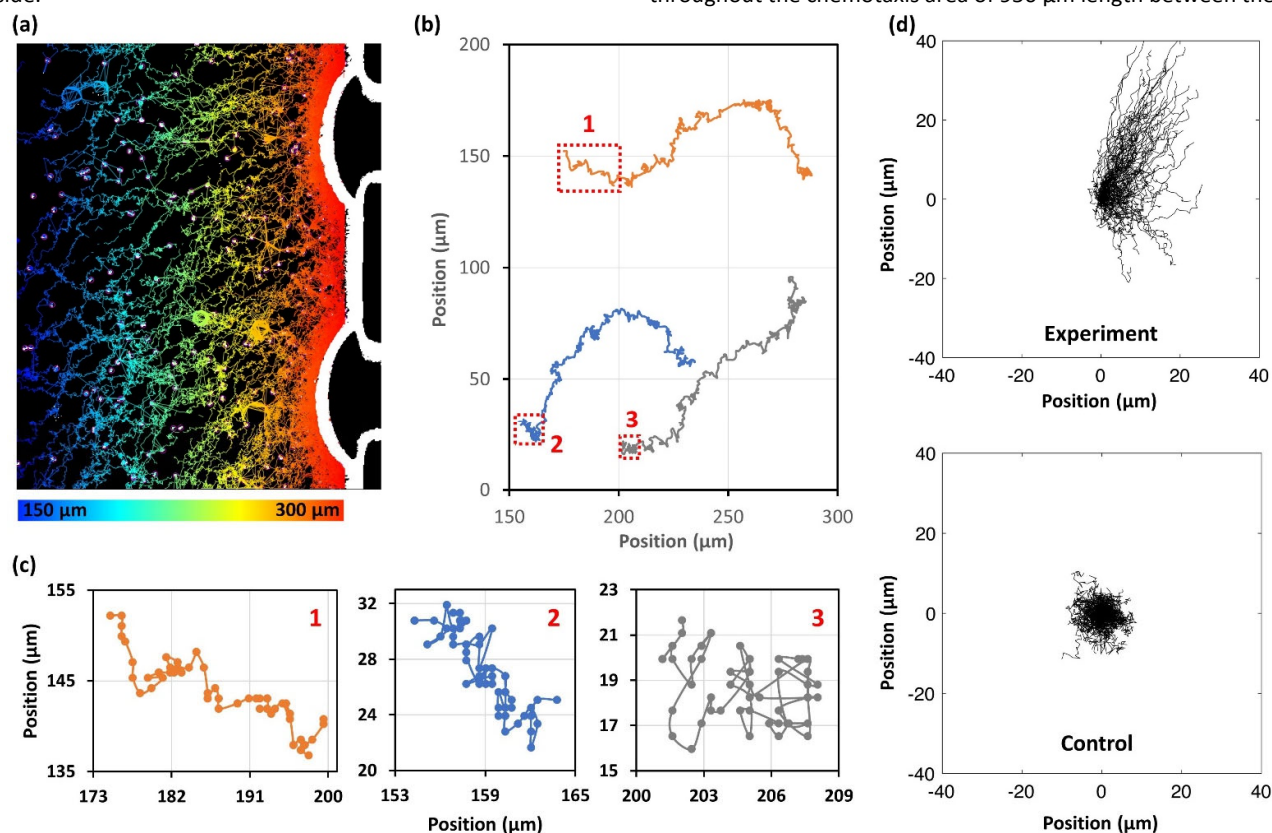


**Figure 5.** Individually tracked chemotactic trajectories of *E. coli* cells and the rose plots. (a) The chemotactic migration paths of individual cells from 10 to 20 minutes under chemotaxis in the glucose section were visualized by connecting the location of every second with unique identification number of each bacterium and the paths were coloured based on location. (b) Three representative trajectories for 10 minutes showing the horizontal orientation of the chemotactic migration. (c) The first minute of the three representative trajectories connecting the locations at each second, showing the biased random walk of bacteria in the presence of chemoattractant gradient. (d) Rose plots of 100 cell trajectories for three seconds under chemoattractant gradient (experiment) and without chemoattractant gradient (control) analysed with TumbleScore.

The second approach using TumbleScore, an algorithm developed in MATLAB for video analysis<sup>50</sup>, to generate rose plots of cells under chemotaxis. Figure 5(d) shows the trajectories of 100 cells for 3 seconds tracked and plotted from

two chitosan membrane arrays (Figure 1(d)). The device could be further improved with degassing air out of PDMS before use to avoid air bubble-induced flow, and careful sealing of the input and output to the middle channels. The tracked cellular

paths could be further examined in more details about the working mechanism of chemotactic migration and directional decision of single cells in different conditions.

Overall, we presented a useful and robust platform with exemplified chemotaxis study of *E. coli* and *P. aeruginosa* cells in static glucose gradients, which provides the unique advantages quantifying cellular behaviors in both population-wise and single cell levels that could solve common challenges in microfluidic-based chemotaxis studies.

#### 4. Conclusions

We report the quantification of adhesion-free bacterial chemotaxis with several advantages under the static chemoattractant gradient generated in a semipermeable membrane-integrated microfluidic platform. A steady and static gradient of chemoattractant was generated and well-maintained in this platform by continuous flows of buffer and chemoattractant solutions in two side channels. To provide the most accurate analysis for characterizing chemotaxis, we specifically targeted often-encountered problems such as flow, cell adhesion, and shear stress. Of particular interest is the flow involved during the initial gradient setup and its propagation throughout the system, which often makes for a long wait time for gradient creation and, at times, erroneous initial conditions. Here, we stop flow by blocking the outlet with a solid metal plug and sealing the inlet with parafilm; this allows us to introduce cells with no initial momentum and no external stress. Second, in related manner we used rapidly assembled chitosan/alginate membranes to limit pressure-driven flows and shear stress. That is, our system limits chemoattractant distribution to chemical diffusion only and this is across chitosan membranes bounding the middle channel. Finally, cell adhesion to the PDMS channel surface is addressed by GA crosslinking of chitosan membranes, which strengthens the anchoring to PDMS, and priming the surface with Pluronic F-127, which enhances PDMS hydrophilicity and limits cell adherence.

With these factors minimized, the measured bacterial chemotactic migration towards glucose (or away from glucose in the *P. aeruginosa* case) was the direct result of the chemoattractant gradient. The calculated coefficients CPC and CMC revealed that half of the bacterial chemotactic migration into the section of high concentration of chemoattractant happened immediately within the first 10 minutes of the chemotaxis assays. Each bacterium was individually tracked, and its chemotactic migration trajectory was visualized, which represented the dynamic random walk of *E. coli* cells in the chemoattractant gradient.

We have recorded and quantified bacterial chemotaxis to glucose with high accuracy and maximal cellular motility under the generated static gradient in a semipermeable membrane-based microfluidic platform. We envision that the biopolymer membrane-integrated platform can be a convenient and robust system with high accuracy for quantitative assessment of cellular mobility such as chemotactic responses in static chemoattractant gradients.

#### Author contributions

The authors confirm contributions to the paper as follows: Conceptualization: W. Bentley, G. Rubloff, H. Sintim, H. Wu and X. Luo; Data curation: P. Hu, K. Ly, L. Pham and X. Luo; Formal Analysis: P. Hu, L. Pham, E. Pottash and X. Luo; Funding acquisition: W. Bentley, G. Rubloff, H. Sintim and X. Luo; Investigation: P. Hu, K. Ly, Le, Pham, K. Sheridan and X. Luo; Methodology and resources: P. Hu, H. Wu, C. Tsao, D. Quan, W. Bentley, G. Rubloff and X. Luo; Visualization and validation: P. Hu, E. Pottash, W. Bentley and X. Luo; Project administration and supervision: W. Bentley, G. Rubloff and X. Luo; Writing – original draft: P. Hu, K. Ly and X. Luo; Writing – review and editing: K. Ly, W. Bentley, H. Wu, C. Tsao and X. Luo. All authors approved the final version of the manuscript.

#### Conflicts of interest

There are no conflicts to declare.

#### Acknowledgements

This work was supported by the National Science Foundation (1264509, CAREER 1553330) and the National Institute of Health (1R15GM129766-01).

#### References

- G. H. Wadhams and J. P. Armitage, *Nature reviews Molecular cell biology*, 2004, **5**, 1024-1037.
- C. J. Wolfram, G. W. Rubloff and X. Luo, *Biomicrofluidics*, 2016, **10**, 061301.
- R. A. Arkowitz, *Cold Spring Harbor perspectives in biology*, 2009, **1**, a001958.
- M. M. Salek, F. Carrara, V. Fernandez, J. S. Guasto and R. Stocker, *Nature communications*, 2019, **10**, 1-11.
- J. Adler, *Science*, 1969, **166**, 1588-1597.
- P. S. Stewart and M. J. Franklin, *Nature Reviews Microbiology*, 2008, **6**, 199-210.
- G. Pandey and R. K. Jain, *Applied and Environmental Microbiology*, 2002, **68**, 5789-5795.
- Z. Xiao-Qian, L. Zhe-Yu, X.-Y. ZHANG, L. Jiang, R. Nan-Qi and S. Kai, *Chinese Journal of Analytical Chemistry*, 2017, **45**, 1734-1744.
- N. S. Forbes, *Nature Reviews Cancer*, 2010, **10**, 785-794.
- J. Song, Y. Zhang, C. Zhang, X. Du, Z. Guo, Y. Kuang, Y. Wang, P. Wu, K. Zou, L. Zou, J. Lv and Q. Wang, *Sci Rep*, 2018, **8**, 6394.
- J. Adler, *Science*, 1966, **153**, 708-716.
- S. Boyden, *The Journal of experimental medicine*, 1962, **115**, 453-466.
- D. Zicha, G. A. Dunn and A. F. Brown, *Journal of cell science*, 1991, **99**, 769-775.
- W. Shang, C.-Y. Tsao, X. Luo, M. Teodoro, R. McKay, D. N. Quan, H.-C. Wu, G. F. Payne and W. E. Bentley, *Biomicrofluidics*, 2017, **11**, 044114.
- X. Wang, Z. Liu and Y. Pang, *RSC advances*, 2017, **7**, 29966-29984.

16. N. Murugesan, P. Dhar, T. Panda and S. K. Das, *Biomicrofluidics*, 2017, **11**, 024108.
17. G. Paduthol, T. S. Korma, A. Agrawal and D. Paul, *Lab on a Chip*, 2022, **22**, 592-604.
18. H. Mao, P. S. Cremer and M. D. Manson, *Proceedings of the National Academy of Sciences*, 2003, **100**, 5449-5454.
19. M. Kim, S. H. Kim, S. K. Lee and T. Kim, *Analyst*, 2011, **136**, 3238-3243.
20. N. L. Jeon, S. K. Dertinger, D. T. Chiu, I. S. Choi, A. D. Stroock and G. M. Whitesides, *Langmuir*, 2000, **16**, 8311-8316.
21. K. P. Kim, Y.-G. Kim, C.-H. Choi, H.-E. Kim, S.-H. Lee, W.-S. Chang and C.-S. Lee, *Lab on a Chip*, 2010, **10**, 3296-3299.
22. S.-Y. Cheng, S. Heilman, M. Wasserman, S. Archer, M. L. Shuler and M. Wu, *Lab on a Chip*, 2007, **7**, 763-769.
23. R. Rusconi, J. S. Guasto and R. Stocker, *Nature physics*, 2014, **10**, 212-217.
24. X. Luo, T. Vo, F. Jambi, P. Pham and J. S. Choy, *Lab on a Chip*, 2016, **16**, 3815-3823.
25. T. Ahmed, T. S. Shimizu and R. Stocker, *Nano letters*, 2010, **10**, 3379-3385.
26. B. Mosadegh, M. Agarwal, H. Tavana, T. Bersano-Begey, Y.-s. Torisawa, M. Morell, M. J. Wyatt, K. S. O'Shea, K. F. Barald and S. Takayama, *Lab on a Chip*, 2010, **10**, 2959-2964.
27. N. Garcia-Seyda, L. Aoun, V. Tishkova, V. Seveau, M. Biarnes-Pelicot, M. Bajenoff, M.-P. Valignat and O. Theodoly, *Lab on a Chip*, 2020, **20**, 1639-1647.
28. Y. Shin, S. Han, J. S. Jeon, K. Yamamoto, I. K. Zervantonakis, R. Sudo, R. D. Kamm and S. Chung, *Nature protocols*, 2012, **7**, 1247-1259.
29. H.-H. Jeong, S.-H. Lee and C.-S. Lee, *Biosensors and Bioelectronics*, 2013, **47**, 278-284.
30. H. Xu, M. M. Ferreira and S. C. Heilshorn, *Lab on a chip*, 2014, **14**, 2047-2056.
31. A. H. Khan, N. M. Smith, M. P. Tullier, B. S. Roberts, D. Englert, J. A. Pojman and A. T. Melvin, *ACS Applied Materials & Interfaces*, 2021, **13**, 26735-26747.
32. W. Shang, C. Y. Tsao, X. Luo, M. Teodoro, R. McKay, D. N. Quan, H. C. Wu, G. F. Payne and W. E. Bentley, *Biomicrofluidics*, 2017, **11**, 044114.
33. S. Suh, M. A. Traore and B. Behkam, *Lab on a Chip*, 2016, **16**, 1254-1260.
34. C. B. Goy, R. E. Chaile and R. E. Madrid, *Reactive and Functional Polymers*, 2019, **145**, 104314.
35. K. Nagy, O. Sipos, S. Valkai, É. Gombai, O. Hodula, Á. Kerényi, P. Ormos and P. Galajda, *Biomicrofluidics*, 2015, **9**, 044105.
36. X. Luo, D. L. Berlin, J. Betz, G. F. Payne, W. E. Bentley and G. W. Rubloff, *Lab on a Chip*, 2010, **10**, 59-65.
37. X. Luo, H.-C. Wu, J. Betz, G. W. Rubloff and W. E. Bentley, *Biochemical engineering journal*, 2014, **89**, 2-9.
38. K. Ly, P. Hu, P. Pham and X. Luo, *Journal of Materials Chemistry B*, 2021, DOI: 10.1039/D1TB00045D.
39. F. Croisier and C. Jérôme, *European Polymer Journal*, 2013, **49**, 780-792.
40. W. Suginta, P. Khunkaewla and A. Schulte, *Chemical reviews*, 2013, **113**, 5458-5479.
41. A. Rafique, K. M. Zia, M. Zuber, S. Tabasum and S. Rehman, *International journal of biological macromolecules*, 2016, **87**, 141-154.
42. Y. Cheng, X. Luo, J. Betz, S. Buckhout-White, O. Bekdash, G. F. Payne, W. E. Bentley and G. W. Rubloff, *Soft Matter*, 2010, **6**, 3177-3183.
43. P. Hu, S. A. Rooholghodos, L. H. Pham, K. L. Ly and X. Luo, *Langmuir*, 2020, **36**, 11034-11043.
44. K. L. Ly, C. B. Raub and X. Luo, *Materials Advances*, 2020, **1**, 34-44.
45. P. Hu, C. B. Raub, J. S. Choy and X. Luo, *Journal of Materials Chemistry B*, 2020, **8**, 2519-2529.
46. P. Pham, T. Vo and X. Luo, *Lab on a Chip*, 2017, **17**, 248-255.
47. K. L. Ly, S. A. Rooholghodos, C. Rahimi, B. Rahimi, D. R. Bienek, G. Kaufman, C. B. Raub and X. Luo, *Biomedical Microdevices*, 2021, **23**, 7.
48. X. Luo, H.-C. Wu, C.-Y. Tsao, Y. Cheng, J. Betz, G. F. Payne, G. W. Rubloff and W. E. Bentley, *Biomaterials*, 2012, **33**, 5136-5143.
49. X. Luo, C.-Y. Tsao, H.-C. Wu, D. N. Quan, G. F. Payne, G. W. Rubloff and W. E. Bentley, *Lab on a Chip*, 2015, **15**, 1842-1851.
50. A. E. Pottash, R. McKay, C. R. Virgile, H. Ueda and W. E. Bentley, *Biotechniques*, 2017, **62**, 31-36.
51. D. L. Englert, M. D. Manson and A. Jayaraman, *Nat Protoc*, 2010, **5**, 864-872.
52. H. Moghadas, M. S. Saidi, N. Kashaninejad and N. T. Nguyen, *Biomicrofluidics*, 2018, **12**, 024117.
53. J. C. Wang, W. Liu, Q. Tu, C. Ma, L. Zhao, Y. Wang, J. Ouyang, L. Pang and J. Wang, *Analyst*, 2015, **140**, 827-836.
54. A. Abay, G. Simionato, R. Chachanidze, A. Bogdanova, L. Hertz, P. Bianchi, E. Van Den Akker, M. Von Lindern, M. Leonetti and G. Minetti, *Frontiers in physiology*, 2019, **10**, 514.
55. Y. Gu, V. Hegde and K. J. Bishop, *Lab on a Chip*, 2018, **18**, 3371-3378.
56. C. Virgile, P. Hauk, H.-C. Wu, W. Shang, C.-Y. Tsao, G. F. Payne and W. E. Bentley, *PLoS One*, 2018, **13**, e0196999.
57. T. L. Pitt and A. J. Simpson, *Principles and practice of clinical bacteriology*, 2006, **2**, 427-435.
58. F. Rojo, *FEMS Microbiol. Rev.*, 2010, **34**, 658-684.
59. A. Daddaoua, T. Krell and J.-L. Ramos, *The Journal of biological chemistry*, 2009, **284**, 21360-21368.
60. I. Bucior, J. Abbott, Y. Song, M. A. Matthey and J. N. Engel, *Am J Physiol Lung Cell Mol Physiol*, 2013, **305**, L352-L363.
61. J. Adler, G. L. Hazelbauer and M. M. Dahl, *J Bacteriol*, 1973, **115**, 824-847.
62. K. Son, F. Menolascina and R. Stocker, *Proceedings of the National Academy of Sciences*, 2016, **113**, 8624-8629.
63. J.-Y. Tinevez, N. Perry, J. Schindelin, G. M. Hoopes, G. D. Reynolds, E. Laplantine, S. Y. Bednarek, S. L. Shorte and K. W. Eliceiri, *Methods*, 2017, **115**, 80-90.
64. A. E. Patteson, A. Gopinath, M. Goulian and P. E. Arratia, *Sci Rep*, 2015, **5**, 15761.